Velocity contrast across the 1944 rupture zone of the North Anatolian fault east of Ismetpasa from analysis of teleseismic arrivals

Yaman Ozakin,[1] Yehuda Ben-Zion,[1] Mustafa Aktar,[2] Hayrullah Karabulut,[2] and Zhigang Peng[3]

Received 20 February 2012; revised 23 March 2012; accepted 27 March 2012; published 26 April 2012.

[1] We use differences between arrival times of teleseismic events at sets of stations crossing the North Anatolian fault east of Ismetpasa, where shallow creep has been observed, to detect and quantify a contrast of seismic velocities across the fault. Waveform cross correlations are utilized to calculate phase delays of *P* waves with respect to expected teleseismic arrivals with incident angles corresponding to the generating events. Compiled delay times associated with 121 teleseismic events indicate about 4.3% average *P* wave velocity contrast across the fault over the top 36 km, with faster velocity on the north side. The estimated contrast is about 8.3% if the velocity contrast is limited to the top 18 km. The sense of velocity contrast is consistent with the overall tectonic setting and inference made for the examined fault section based on theoretical expectations for bimaterial ruptures and observed asymmetry of rock damage across the fault. Our data indicate lack of significant microseismicity near the fault, suggesting that creep in the area is limited to the depth section above the seismogenic zone. **Citation:** Ozakin, Y., Y. Ben-Zion, M. Aktar, H. Karabulut, and Z. Peng (2012), Velocity contrast across the 1944 rupture zone of the North Anatolian fault east of Ismetpasa from analysis of teleseismic arrivals, *Geophys. Res. Lett.*, *39*, L08307, doi:10.1029/2012GL051426.

1. Introduction

[2] Active faulting over geological time brings into contact materials that were originally separated and are thus likely to have different elastic properties. Geological studies show that the principal slip zone in large fault structures is often localized along bimaterial interfaces that separate rock units with considerably different properties [e.g., *Sengor et al.*, 2005; *Dor et al.*, 2008; *Mitchell et al.*, 2011]. Bimaterial interfaces can have a number of important roles in earthquake and fault zone seismology. A lithology contrast in earthquake source regions produces an ambiguity in inferred seismic moments, associated with the multiple available choices for the assumed rigidity [e.g., *Ben-Zion*, 1989; *Heaton and Heaton*, 1989]. Earthquake ruptures on a bimaterial interface may propagate as a pulse with a preferred propagation direction [e.g., *Weertman*, 1980; *Ben-Zion and Andrews*, 1998; *Zaliapin and Ben-Zion*, 2011; *Lengline and Got* 2011]. Ignoring a velocity contrast across the fault can produce biases and errors in derived earthquake locations, fault plane solutions, and other source and structure properties [e.g., *McNally and McEvilly*, 1977; *Oppenheimer et al.*, 1988; *Ben-Zion and Malin*, 1991; V. Schulte-Pelkum and Y. Ben-Zion, Apparent vertical Moho offsets under continental strike-slip faults from lithology contrasts in the seismogenic crust, manuscript in preparation, 2012].

[3] The most diagnostic information on bimaterial interfaces can be obtained from fault zone head waves that propagate along, and hence owe their existence to, velocity contrast interfaces [e.g., *Ben-Zion*, 1989, 1990]. Using head waves is best done with record sections of seismograms generated by numerous earthquakes on the fault of interest and observed at near-fault stations [e.g., *McGuire and Ben-Zion*, 2005; *Zhao et al.*, 2010]. Since dense near-fault seismic data are not always available, it is desirable to develop simple techniques that could be used to image fault bimaterial interfaces with more commonly available data. In the present paper we develop and use such a method based on teleseismic arrivals at stations on the opposite sides of a fault. The study is done in the context of the 1944 M7.3 earthquake rupture zone on the North Anatolian fault (NAF).

[4] Ruptures on a bimaterial interface having a high angle to the maximum compressive background stress, which is representative for large continental strike-slip faults, is expected to produce [e.g., *Ben-Zion and Shi*, 2005] significantly more shallow off-fault damage on the stiffer side of the fault. *Dor et al.* [2008] performed detailed mapping of rock damage along several sections of the NAF including the 1944 rupture zone. From clear asymmetry of rock damage, they suggested that the north side of the 1944 rupture zone has faster seismic velocity at seismogenic depth than the south side. In this paper we test this inference using seismic data recorded by a small seismic array across the surface trace of the 1944 rupture east of Ismetpasa. In the next section we describe briefly the experiment and basic properties of the data set. In section 3 we outline the employed imaging method. The results are presented in section 4 and discussed in section 5.

2. Seismic Experiment and Data

[5] We conducted a small seismic experiment in the region of the 1944 rupture of the NAF east of Ismetpasa with

[1]Department of Earth Sciences, University of Southern California, Los Angeles, California, USA.
[2]Kandilli Observatory, Bogazici University, Istanbul, Turkey.
[3]School of Earth and Atmospheric Sciences, Georgia Institute of Technology, Atlanta, Georgia, USA.

Corresponding Author: Y. Ozakin, Department of Earth Sciences, University of Southern California, 3651 Trousdale Pkwy. #B15, Los Angeles, CA 90089-0740, USA. (dandik@gmail.com)

0094-8276/12/2012GL051426

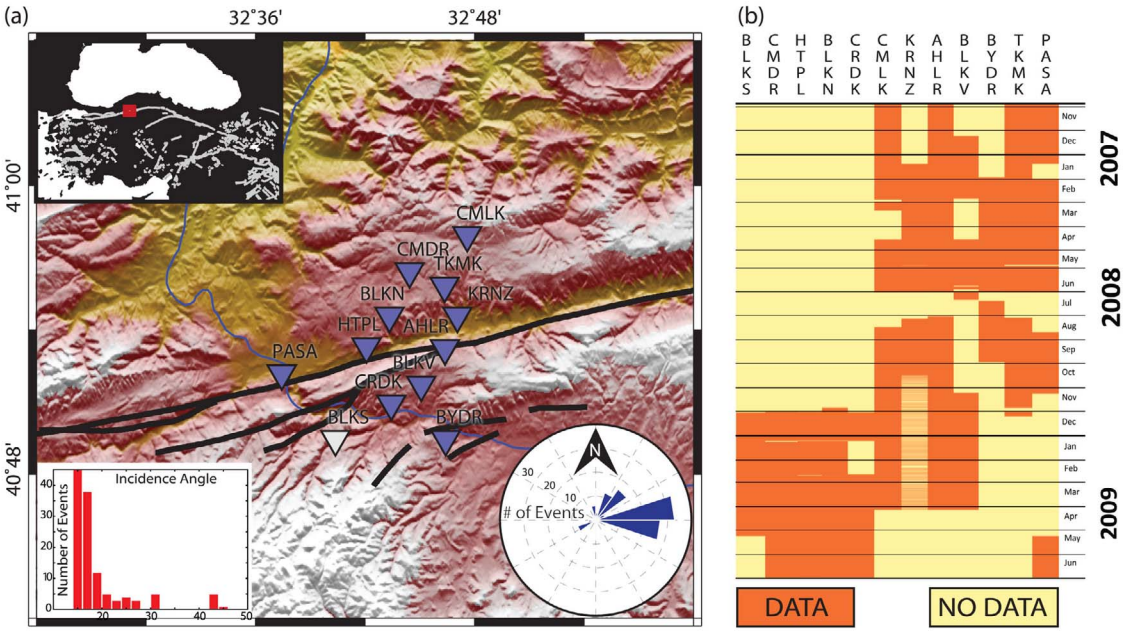

Figure 1. (a) Map of the seismic stations (blue triangles) across the North Anatolian fault zone (black line) east of Ismetpasa used in this study. One station (white triangle) did not record sufficient high quality data (see text) and was not used. The bottom insets show the back-azimuth and incidence angle distributions of the used events. The top inset has a large-scale map. The background colors indicate topography with white being high and red/brown/green being low. (b) Summary of data coverage at different stations.

a line of 6–12 seismometers that cross the fault (Figure 1a). The network operated for about 2 years with different periods of recording at different stations (Figure 1b). The instruments were a mixture of Guralp 40 T seismometers with Reftek 130 recorders and Guralp 6TD integrated seismometer plus digitizers. All stations were deployed in bedrocks with comparable (best possible) site conditions. The position and elevation of the stations are listed in Table S1 in the auxiliary material.[1] The location of the experiment was chosen because it is within the area where *Dor et al.* [2008] found strong asymmetry of rock damage that may reflect repeating ruptures with preferred propagation direction on a bimaterial interface. The location also coincides with a section of the NAF that is partially creeping at least at shallow depth. The creep rate decayed from a maximum of 4–6 cm/yr following the 1944 earthquake to a present value of 0.7 cm/yr [*Cakir et al.*, 2005].

[6] Earthquake detection in the recorded data was done by a manual inspection of automatic identification of candidate events. The events were located using the code hypo and the velocity model of *Cambaz and Karabulut* [2010]. To date we were able to detect only ~235 events in the magnitude range −1 to 2.5 within a radius of 45 km from the center of the network. Only 15–20 events are located within 3 km of the fault and they all have $M_L < 1.0$. Using these as templates for detecting more events was not successful so far as the signals produced by these events are close to the background noise. The small number of events close to the fault is in marked contrast to the numerous microearthquakes [e.g., *Hill et al.*, 1990] along the creeping section of the San Andreas fault (SAF), suggesting that the NAF east of Ismetpasa does not creep at seismogenic depth. Given the small number of local earthquakes, we use teleseismic data to detect and quantify the possible existence of different rock bodies across the fault.

3. Using Teleseismic Arrivals to Image Velocity Contrast Across A Fault

[7] The basic data processing in this study is done with the ObsPy toolkit [*Beyreuther et al.*, 2010]. Teleseismic waves which arrive with near-vertical incidence angles sample the crustal structures below the stations. We calculate the expected arrival times of such teleseismic waves in the absence of a velocity contrast across the fault with the TauP toolkit [*Crotwell et al.*, 1999]. The calculations account for differences in arrival times related to the geometry of the stations and incoming planar teleseismic waves (Figure 2). If the crustal structures across the fault are different, this should be manifested by systematic differences between the actual arrivals and expectations at stations on the opposite sides of the fault. We assume that there is no velocity contrast in the mantle.

[8] For each pair of stations, we compile a data set consisting of the differences (Figure 2a) between the observed and estimated arrivals at the two stations, $\Delta t_{1-2} = \Delta t_1 - \Delta t_2$, using all available teleseismic arrivals at the stations. The differences of teleseismic arrival times are measured using waveform cross correlations. Figure 3a shows example results of Δt_{1-2} values associated with stations AHLR and CMLK. If the number of observations for a given data set

[1]Auxiliary materials are available in the HTML. doi:10.1029/2012GL051426.

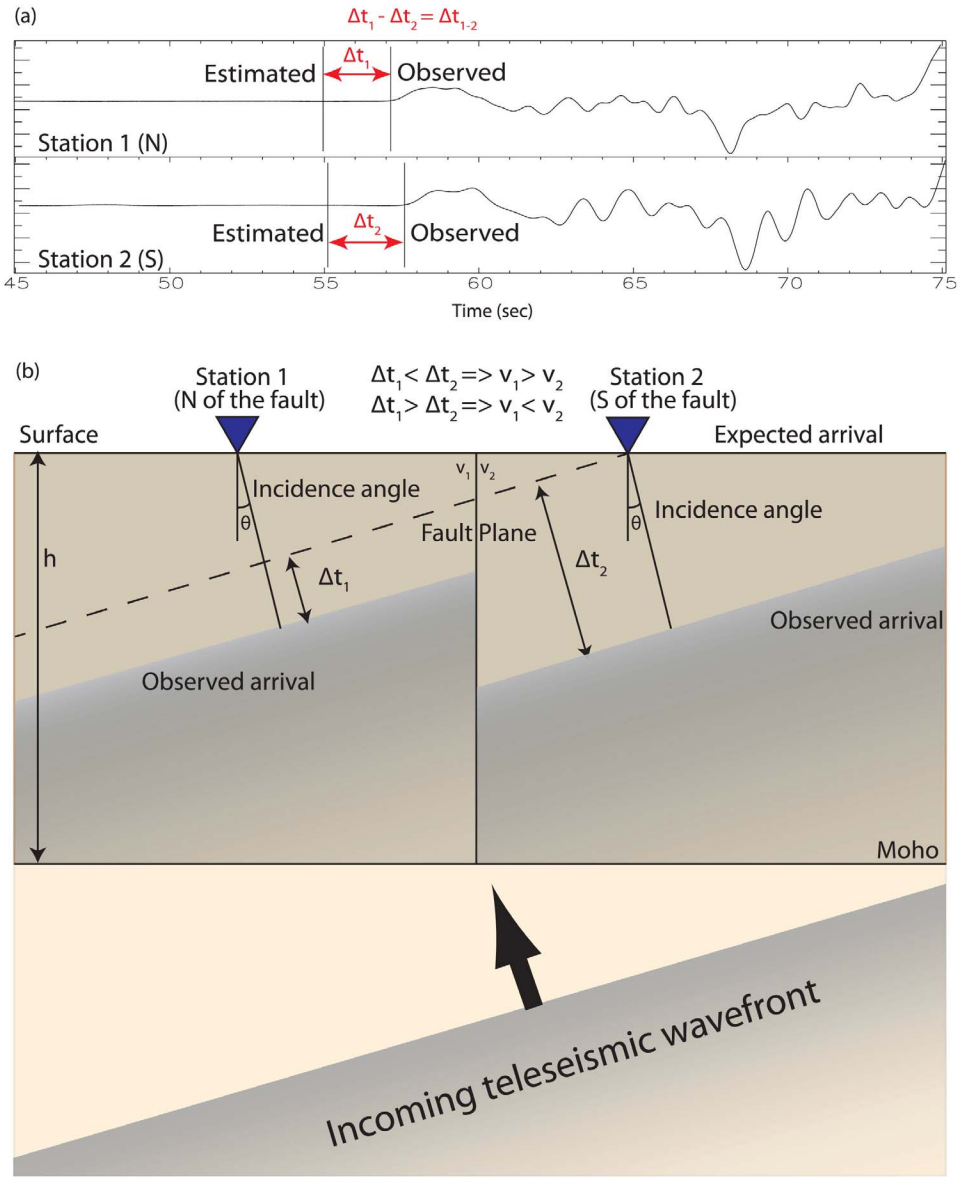

Figure 2. (a) Example waveforms observed at stations BLKN and BLKV located north and south of the fault, respectively. (b) Illustration of differences between arrival times of teleseismic waves with incidence angle θ and reference expectations at stations across the fault. Systematic earlier arrivals on a given side of the fault indicate faster seismic velocities. See text for additional details.

(pair of stations) is less than 5, or the standard deviation of the measured arrival time differences is greater than 0.15 sec, the data set is deemed not having sufficient quality and is ignored. The adopted thresholds for data quality are somewhat arbitrary, but the obtained results are not very sensitive to the used values. This procedure provides 42 data sets of arrival time differences (Figure S1 in the auxiliary material) that are used for further analysis.

[9] To estimate the velocity contrast between a given pair of stations, we use a reference constant crustal thickness h and average crustal P wave velocities beneath the two stations v_1 and v_2. The incidence angles of waves are generally station-dependent, but because teleseismic data are used we assume that the angles at the different stations are essentially the same. From the basic geometry illustrated in Figure 2b, the travel time difference of a planar teleseismic wave with incidence angle θ at the two stations is

$$\Delta t_{1-2} = \frac{h}{v_1 \cos(\theta)} - \frac{h}{v_2 \cos(\theta)}. \quad (1)$$

The corresponding ratio of the average crustal velocities beneath the two stations is

$$\frac{v_1}{v_2} = \frac{h}{h + \Delta t_{1-2} v_2 \cos(\theta)}. \quad (2)$$

Equation (2) is used to convert the time differences in each data set (Figures 3a and S1) to velocity ratios (Figure 3b). The mean of the calculated ratios is assigned to the

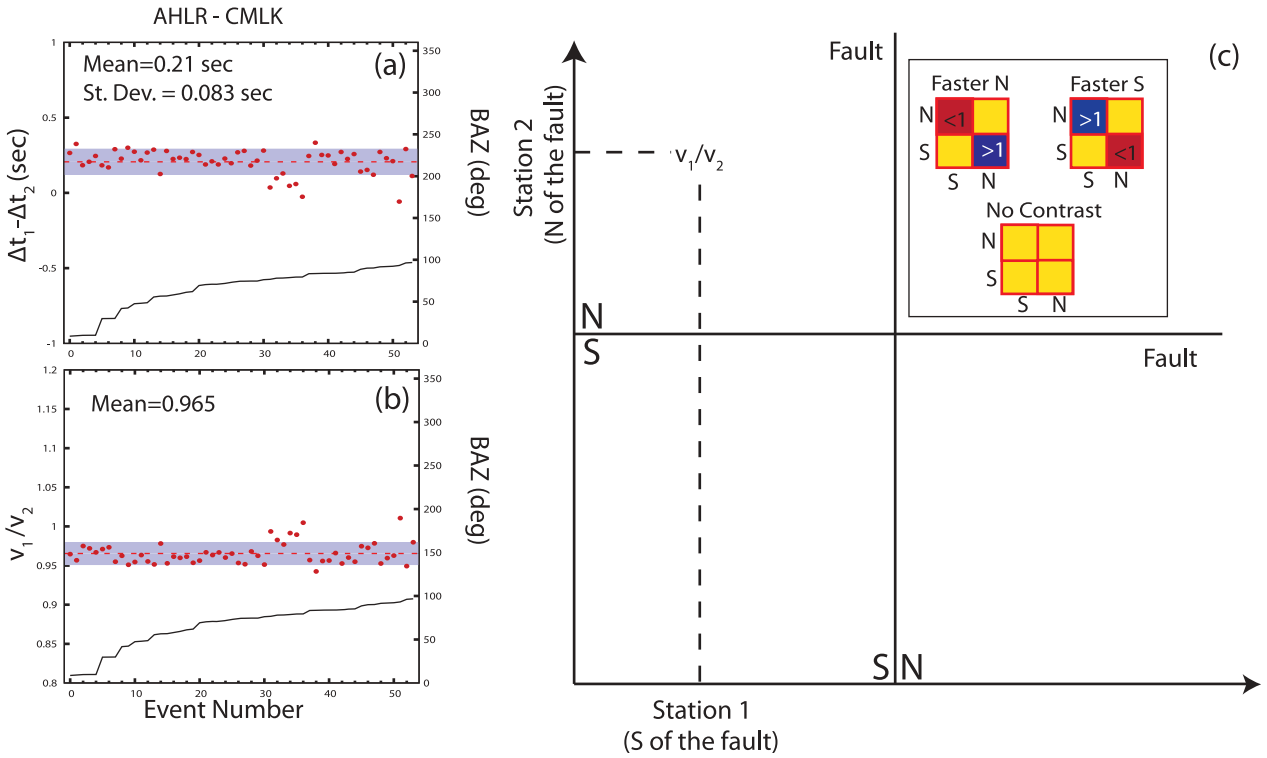

Figure 3. Illustration of the method used to compile data on contrast of seismic velocity across the fault. (a) Arrival time differences (dots) between observations at stations AHLR and CMLK for all teleseismic events recorded at both stations. The horizontal line and shaded band denote, respectively, the mean with one standard-deviation on each side. The events are sorted by back-azimuth shown by the black line and scale on the right. (b) Corresponding results for velocity ratios based on the arrival time differences in Figure 3a and equation (2). (c) A 4-qudrant diagram with stations sorted on both axes from north to south. A location in the chart indicates the relevant pairs of stations and the color at that point indicates the velocity ratio. (Inset) Clusters of ratios greater or smaller than one in two diagonal quadrants are indicative of a velocity contrast across the fault.

associated pair of stations. Example set of estimated velocity ratios is shown in Figure 3b, assuming that h = 36 km (Y. Ozakin and M. Aktar, The Moho topography of Turkey from P-receiver functions, submitted to *Journal of Geophysical Research*, 2012) and v_2 = 6.8 km/s [*Cambaz and Karabulut*, 2010]. Analogous results obtained for all pairs of stations are used to construct a matrix of velocity ratios at different positions (Figure 3c). The matrix is indexed using stations that are sorted by distances from the fault where stations on the north side have positive coordinates. A value less than 1.0 in the matrix indicates that the velocity beneath the station of the relevant column is smaller than the one beneath the station in the corresponding row. If the velocity ratios between stations on the north and south sides are systematically greater than 1.0, the crustal section to the north should be on the average faster and vice versa (assuming the crustal thickness does not vary too much across the fault). If such relations hold when comparing all station pairs that are on the opposite sides of the fault, we should get clusters of positive and negative values in corresponding quadrants of the matrix.

[10] Based on a receiver function study (Ozakin and Aktar, submitted manuscript, 2012), the average crustal thickness in our study area is 36 km and there is an average increase of the crustal thickness of about 1.5–2.0 km over a distance of 100 km from north to south (assuming smooth thickness variation). The NS extent of the network is about 20 km, giving about 0.3–0.4 km of potential crustal thickness variations. With an average P wave velocity of 6.8 km/s [*Cambaz and Karabulut*, 2010], this corresponds to less than 0.1 sec difference in arrival times. These values are sufficiently small not to affect the results obtained in the next section.

4. Results

[11] We use 121 teleseismic events between 2007 and 2009 taken from the USGS web site http://earthquake.usgs.gov/earthquakes/eqarchives/epic/epic_global.php (Table S2 in the auxiliary material). The great circle distances (Δ in degrees) of the teleseismic events are converted to incidence angles using the relation

$$\theta = 0.00383\Delta^2 - 0.72\Delta + 49.33. \quad (3)$$

This expression is based on least-squares fit to travel time calculations in a layered earth model [Lay and Wallace, 1995, Table 8.1]. Most incidence angles of the employed data are $\theta \leq 25°$ (Figure 1a, bottom left), consistent with our assumption of near vertical propagation. Eliminating the data associated with $\theta > 25°$ does not change appreciably the estimated velocity contrast values.

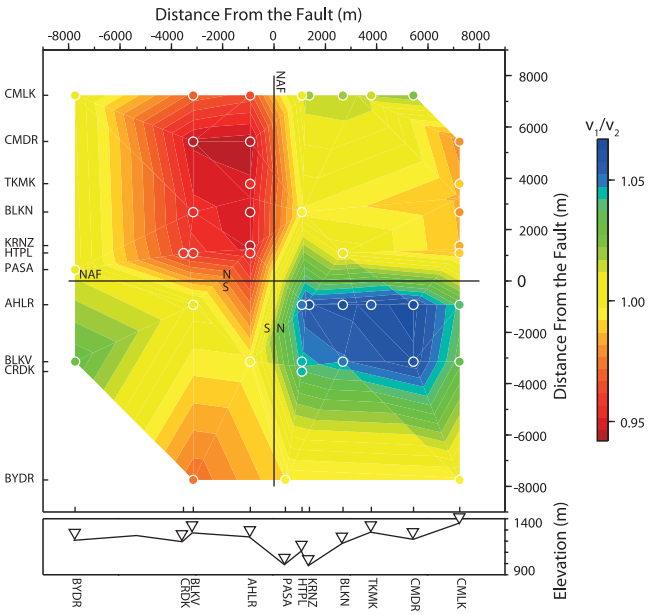

Figure 4. (top) Velocity ratios (colors) based on time differences between teleseismic arrivals and reference expectations at pairs of stations as illustrated in Figure 3. The circles with white outline denote velocity ratios for all pairs of stations and the smooth color map is a Delaunay mesh of block-mean of data points. The observed coherent colors in the top-left and bottom-right quadrants indicate that the north side of the fault has faster *P* wave velocity. (bottom) Elevations of stations used in the study. See text for additional details.

[12] Figure 4 shows a color map of velocity contrast ratios obtained by interpolating the ratios derived for all pairs of stations as discussed before (Figure 3) using h = 36 km and v_2 = 6.8 km/s. The results have clear clusters of ratios larger and smaller than 1.0 indicative of a velocity contrast across the fault. Specifically, the upper left quadrant indicates velocity ratios between stations on the south (along the horizontal axis) and stations on the north (along the vertical axis). The general existence of ratios less than 1.0 in this quadrant implies that the average crustal *P* velocity in the south is smaller than in the north. Similar information is given in a slightly different geometrical form at the bottom right quadrant. With h = 36 km and v_2 = 6.84 km/s, the average velocity contrast across the fault is 4.3%. The differences in station elevations (Figure 4, bottom) are unlikely to affect significantly the obtained results, as the elevation changes across the fault are smaller than the internal variations on the north side. Figure S2 in the auxiliary material shows that there is no clear correlation between the obtained velocity contrast and station elevations.

5. Discussion

[13] We developed and implemented a simple method to estimate the average contrast of crustal seismic velocities across a fault from teleseismic arrivals at several stations on the opposite sides of the fault. As mentioned in the introduction, a lithology contrast across a fault can influence the directivity of earthquake ruptures (and hence expected shaking hazard in different along-strike directions), and may be relevant for various other aspects of fault mechanics and seismology [e.g., *Ben-Zion and Andrews*, 1998; *Oppenheimer et al.* 1988]. In many places dense seismic networks do not exist and it is important to develop simple tools that may be used to detect and provide first-order estimates of velocity contrasts across faults. Our method provides such a tool, which may be used with a small number of stations across faults that are in seismically quiet periods.

[14] Some background information is needed to reduce the non-uniqueness associated with trade-offs between changes of crustal thickness and velocity contrast across a fault, as done in the present study based on the results of Ozakin and Aktar (submitted manuscript, 2012). We note that standard receiver function studies, ignoring the possible existence of lithology variation across the fault, tend to overestimate changes of crustal thickness across the fault (Schulte-Pelkum and Ben-Zion, manuscript in preparation, 2012). Therefore, our estimate of a possible bias assuming constant crustal thickness is likely an upper bound. A support for our interpretation in terms of velocity contrast is provided by the fact that the estimated contrast values generally increase, within fluctuations, as one uses pairs of stations that are progressively closer to the fault. Also, a change in the Moho depth near the fault is expected to broaden the surface deformation [*Lyakhovsky and Ben-Zion*, 2009], whereas the observed deformation in the study area is highly localized [*Cakir et al.*, 2005].

[15] Our results indicate that the average velocity contrast in the top 36 km across the NAF east of Ismetpasa using all stations is 4.3%. Using only the 2 stations just north and south of the fault with similar elevation (BLKN and AHLR), yields an estimated contrast value of about 5.2%. The velocity contrast is expected to decrease with depth [e.g., *Ben-Zion et al.*, 1992; *Lewis et al.*, 2007; *Roux et al.*, 2011]. Assuming for example that the velocity contrast is limited to the upper 18 km of the crust, and using for that depth section v_2 = 6.3 km/s [*Cambaz and Karabulut*, 2010] gives an average contrast value of 8.3%. This is similar to values found for several sections of the SAF [e.g., *McGuire and Ben-Zion*, 2005; *Zhao et al.*, 2010]. The obtained sense of velocity contrast in our study area is consistent with the inference made by *Dor et al.* [2008] in the context of bimaterial ruptures based on observed asymmetry of rock damage, as well as the large scale geological framework associated with the NAF [*Sengor et al.*, 2005]. Detailed analysis of shear wave anisotropy close to the NAF [*Peng and Ben-Zion*, 2004, 2005] does not indicate strong systematic differences between the blocks on the opposite sides of the fault. The average difference of *P* anisotropy across the fault (if such exists) is likely to be even smaller, so anisotropy is unlikely to influence our results significantly.

[16] The best diagnostic signals for imaging fault bimaterial interfaces are head waves generated by seismicity that is localized on a fault [e.g., *Ben-Zion and Malin*, 1991]. Based on our detection efforts to date, the seismic records during the ~2 yr of our experiment (Figure 1) contain very few events near the NAF down to M_L < 1.0. This is in marked contrast to the creeping section of the SAF [e.g., *Hill et al.*, 1990], and the Hayward fault in CA [e.g., *Schmidt et al.*, 2005] which is partially creeping as the NAF fault section examined in this study. *Bulut et al.* [2012] used

recently changes in polarizations of waves in early *P* waveforms to detect fault zone head waves and measure the arrival times of the *P* head and regular body waves. This method can be used (as the one used in our study) with a small number of stations, but it requires again seismicity on the fault. Noise-based techniques can be used to provide structural images in places without seismicity [e.g., *Shapiro et al.*, 2005; *Roux et al.*, 2011]. Future studies using a combination of these and other techniques can improve on the results of this paper.

[17] **Acknowledgments.** The study was funded by the Bogazici University Research Foundation (grant 09M103) and the National Science Foundation (grant EAR-0823695). YBZ acknowledges support from the Alexander von Humboldt foundation. ZP acknowledges support from the Georgia Tech Research Foundation. The paper benefitted from highly useful comments by two anonymous referees.

[18] The Editor thanks the two anonymous reviewers for assisting with the evaluation of this paper.

References

Ben-Zion, Y. (1989), The response of two joined quarter spaces to SH line sources located at the material discontinuity interface, *Geophys. J. Int.*, *98*, 213–222, doi:10.1111/j.1365-246X.1989.tb03346.x.

Ben-Zion, Y. (1990), The response of two half spaces to point dislocations at the material interface, *Geophys. J. Int.*, *101*, 507–528, doi:10.1111/j.1365-246X.1990.tb05567.x.

Ben-Zion, Y., and P. Malin (1991), San Andreas fault zone head waves near Parkfield, California, *Science*, *251*, 1592–1594.

Ben-Zion, Y., S. Katz, and P. Leary (1992), Joint inversion of fault zone head waves and direct P arrivals for crustal structure near major faults, *J. Geophys. Res.*, *97*, 1943–1951.

Ben-Zion, Y., and D. J. Andrews (1998), Properties and implications of dynamic rupture along a material interface, *Bull. Seismol. Soc. Am.*, *88*, 1085–1094.

Ben-Zion, Y., and Z. Shi (2005), Dynamic rupture on a material interface with spontaneous generation of plastic strain in the bulk, *Earth Planet. Sci. Lett.*, *236*, 486–496, doi:10.1016/j.epsl.2005.03.025.

Beyreuther, M., R. Barsch, L. Krischer, T. Megies, Y. Behr, and J. Wassermann (2010), ObsPy: A Python toolbox for seismology, *Seismol. Res. Lett.*, *81*(3), 530–533, doi:10.1785/gssrl.81.3.530.

Bulut, F., Y. Ben-Zion, and M. Bonhoff (2012), Evidence for a bimaterial interface along the Mudurnu segment of the North Anatolian Fault Zone from P wave arrival times and polarization analysis, *Earth Planet. Sci. Lett.*, *327–328*, 17–22, doi:10.1016/j.epsl.2012.02.001.

Cakir, Z., A. M. Akoglu, S. Belabbes, S. Erginav, and M. Meghraoui (2005), Creeping along the Ismetpasa section of the North Anatolian fault (western Turkey): Rate and extent from InSAR, *Earth Planet. Sci. Lett.*, *238*, 225–234, doi:10.1016/j.epsl.2005.06.044.

Cambaz, M. D., and H. Karabulut (2010), Love-wave group velocity maps of Turkey and surrounding regions, *Geophys. J. Int.*, *181*, 502–520, doi:10.1111/j.1365-246X.2010.04516.x.

Crotwell, H. P., T. J. Owens, and J. Ritsema (1999), The TauP Toolkit: Flexible seismic travel-time and ray-path utilities, *Seismol. Res. Lett.*, *70*, 154–160, doi:10.1785/gssrl.70.2.154.

Dor, O., C. Yildirim, T. K. Rockwell, Y. Ben-Zion, O. Emre, M. Sisk, and T. Y. Duman (2008), Geologic and geomorphologic asymmetry across the rupture zones of the 1943 and 1944 earthquakes on the North Anatolian Fault: Possible signals for preferred earthquake propagation direction, *Geophys. J. Int.*, *173*, 483–504, doi:10.1111/j.1365-246X.2008.03709.x.

Heaton, H. T., and R. E. Heaton (1989), Static deformation from point forces and force couples located in welded elastic Poissonian half-spaces: Implications for seismic moment tensors, *Bull. Seismol. Soc. Am.*, *79*, 813–841.

Hill, D. P., J. R. Eaton, and L. M. Johns (1990), Seismicity, 1980–86, in *The San Andreas Fault System, California*, edited by R. Wallace, *U. S. Geol. Surv. Prof. Pap.*, *1515*, 115–151.

Lay, T., and T. C. Wallace (1995), *Modern Global Seismology*, 348 pp., Academic Press, San Diego, Calif.

Lengline, O., and J.-L. Got (2011), Rupture directivity of micro-earthquake sequences near Parkfield, California, *Geophys. Res. Lett.*, *38*, L08310, doi:10.1029/2011GL047303.

Lewis, M. A., Y. Ben-Zion, and J. McGuire (2007), Imaging the deep structure of the San Andreas Fault south of Hollister with joint analysis of fault-zone head and direct *P* arrivals, *Geophys. J. Int.*, *169*, 1028–1042, doi:10.1111/j.1365-246X.2006.03319.x.

Lyakhovsky, V., and Y. Ben-Zion (2009), Evolving geometrical and material properties of fault zones in a damage rheology model, *Geochem. Geophys. Geosyst.*, *10*, Q11011, doi:10.1029/2009GC002543.

McGuire, J., and Y. Ben-Zion (2005), High-resolution imaging of the Bear Valley section of the San Andreas Fault at seismogenic depths with fault-zone head waves and relocated seismicity, *Geophys. J. Int.*, *163*, 152–164, doi:10.1111/j.1365-246X.2005.02703.x.

McNally, K. C., and T. V. McEvilly (1977), Velocity contrast across the San Andreas Fault in central California, small-scale variations from *P*-wave nodal plane distortion, *Bull. Seismol. Soc. Am.*, *67*, 1565–1576.

Mitchell, T. M., Y. Ben-Zion, and T. Shimamoto (2011), Pulverized fault rocks and damage asymmetry along the Arima-Takatsuki Tectonic Line, Japan, *Earth Planet. Sci. Lett.*, *308*, 284–297, doi:10.1016/j.epsl.2011.04.023.

Oppenheimer, D. H., P. A. Reasenberg, and R. W. Simpson (1988), Fault plane solutions for the 1984 Morgan Hill, California, earthquake sequence: Evidence for the state of stress on the Calaveras fault, *J. Geophys. Res.*, *93*, 9007–9026, doi:10.1029/JB093iB08p09007.

Peng, Z., and Y. Ben-Zion (2004), Systematic analysis of crustal anisotropy along the Karadere-Düzce branch of the north Anatolian fault, *Geophys. J. Int.*, *159*, 253–274, doi:10.1111/j.1365-246X.2004.02379.x.

Peng, Z., and Y. Ben-Zion (2005), Spatio-temporal variations of crustal anisotropy from similar events in aftershocks of the 1999 M7.4 İzmit and M7.1 Düzce, Turkey, earthquake sequences, *Geophys. J. Int.*, *160*(3), 1027–1043, doi:10.1111/j.1365-246X.2005.02569.x.

Roux, P., M. Wathelet, and A. Roueff (2011), The San Andreas Fault revisited through seismic-noise and surface-wave tomography, *Geophys. Res. Lett.*, *38*, L13319, doi:10.1029/2011GL047811.

Schmidt, D. A., R. Bürgmann, R. M. Nadeau, and M. A. d'Alessio (2005), Distribution of aseismic slip-rate on the Hayward fault inferred from seismic and geodetic data, *J. Geophys. Res.*, *110*, B08406, doi:10.1029/2004JB003397.

Sengor, A. M. C., O. Tuysuz, C. Imren, M. Sakıınc, H. Eyidogan, N. Gorur, X. Le Pichon, and C. Rangin (2005), The North Anatolian Fault: A new look, *Annu. Rev. Earth Planet. Sci.*, *33*, 37–112, doi:10.1146/annurev.earth.32.101802.120415.

Shapiro, N. M., M. Campillo, L. Stehly, and M. H. Ritzwoller (2005), High resolution surface wave tomography from ambient seismic noise, *Science*, *307*, 1615–1618, doi:10.1126/science.1108339.

Weertman, J. (1980), Unstable slippage across a fault that separates elastic media of different elastic constants, *J. Geophys. Res.*, *85*, 1455–1461, doi:10.1029/JB085iB03p01455.

Zaliapin, I., and Y. Ben-Zion (2011), Asymmetric distribution of aftershocks on large faults in California, *Geophys. J. Int.*, *185*, 1288–1304, doi:10.1111/j.1365-246X.2011.04995.x.

Zhao, P., Z. Peng, Z. Shi, M. Lewis, and Y. Ben-Zion (2010), Variations of the velocity contrast and rupture properties of M6 earthquakes along the Parkfield section of the San Andreas Fault, *Geophys. J. Int.*, *180*, 765–780, doi:10.1111/j.1365-246X.2009.04436.x.